

# **Central Lancashire Online Knowledge (CLoK)**

Title	Alloy design by tailoring phase stability in commercial Ti alloys.
Туре	Article
URL	https://clok.uclan.ac.uk/id/eprint/38146/
DOI	https://doi.org/10.1016/j.msea.2021.141229
Date	2021
Citation	Zhao, GH., Liang, X.Z., Xu, X., Gamza, Monika, Mao, H., Louzguine-Luzgin, D.V. and Rivera-Díaz-del-Castillo, P.E.J. (2021) Alloy design by tailoring phase stability in commercial Ti alloys. Materials Science & Engineering A, 815 (141229). pp. 1-10. ISSN 2161-6213
Creators	Zhao, GH., Liang, X.Z., Xu, X., Gamza, Monika, Mao, H., Louzguine-Luzgin, D.V. and Rivera-Díaz-del-Castillo, P.E.J.

It is advisable to refer to the publisher's version if you intend to cite from the work. https://doi.org/10.1016/j.msea.2021.141229

For information about Research at UCLan please go to <a href="http://www.uclan.ac.uk/research/">http://www.uclan.ac.uk/research/</a>

All outputs in CLoK are protected by Intellectual Property Rights law, including Copyright law. Copyright, IPR and Moral Rights for the works on this site are retained by the individual authors and/or other copyright owners. Terms and conditions for use of this material are defined in the <a href="http://clok.uclan.ac.uk/policies/">http://clok.uclan.ac.uk/policies/</a>

ELSEVIER

Contents lists available at ScienceDirect

# Materials Science & Engineering A

journal homepage: http://www.elsevier.com/locate/msea





# Alloy design by tailoring phase stability in commercial Ti alloys

G.-H. Zhao <sup>a,g</sup>, X.Z. Liang <sup>a</sup>, X. Xu <sup>b,h,i</sup>, M.B. Gamża <sup>c</sup>, H. Mao <sup>d,e</sup>, D.V. Louzguine-Luzgin <sup>f,j</sup>, P.E. J. Rivera-Díaz-del-Castillo <sup>a,\*</sup>

- <sup>a</sup> Department of Engineering, Lancaster University, UK
- <sup>b</sup> Department of Materials, Imperial College London, UK
- <sup>c</sup> Jeremiah Horrocks Institute for Mathematics, Physics and Astrophysics, University of Central Lancashire, UK
- <sup>d</sup> Department of Materials Science and Engineering, KTH Royal Institute of Technology, Sweden
- <sup>e</sup> Thermo-Calc Software AB, Sweden
- f WPI Advanced Institute for Materials Research, Tohoku University, Japan
- g Department of Engineering Science, University of Oxford, UK
- h School of Materials, Sun Yat-Sen University (Shenzhen), China
- <sup>i</sup> Southern Marine Science and Engineering Guangdong Laboratory (Zhuhai), China
- <sup>j</sup> Mathematics for Advanced Materials-OIL, National Institute of Advanced Industrial Science and Technology (AIST), Japan

#### ARTICLE INFO

#### Keywords: Ti alloys Physical modelling Alloy design Phase transformation Plasticity

#### ABSTRACT

The mechanical characteristics and the operative deformation mechanisms of a metallic alloy can be optimised by explicitly controlling phase stability. Here an integrated thermoelastic and pseudoelastic model is presented to evaluate the  $\beta$  stability in Ti alloys. The energy landscape of  $\beta \rightarrow \alpha'/\alpha''$  martensitic transformation was expressed in terms of the dilatational and transformational strain energy, the Gibbs free energy change, the external mechanical work as well as the internal frictional resistance. To test the model, new alloys were developed by tailoring two base alloys, Ti–6Al–4V and Ti–6Al–7Nb, with the addition of  $\beta$ -stabilising element Mo. The alloys exhibited versatile mechanical behaviours with enhanced plasticity. Martensitic nucleation and growth was fundamentally dominated by the competition between elastic strain energy and chemical driving force, where the latter term tends to lower the transformational energy barrier. The model incorporates thermodynamics and micromechanics to quantitatively investigate the threshold energy for operating transformation-induced plasticity and further guides alloy design.

#### 1. Introduction

The thermodynamics and micromechanics of phase stability are fundamental to design Ti alloys displaying effects such as twinning-induced plasticity (TWIP), transformation-induced plasticity (TRIP), shape memory and superelasticity [1–3]. The beta-type Ti alloys are arguably the most versatile in the Ti family [4–6], and widely applied in safety-critical aerospace components [7,8]. From the introduction of Ti–13V–11Cr–3Al (wt.%) as an airframe alloy in the early 1960s, several  $\beta$ -Ti alloys were committed to the aerospace sector such as Ti–10V–2Fe–3Al, Ti–15V–3Al–3Sn–3Cr and Ti–3Al–8V–6Cr–4Mo–4Zr (Beta C) [9,10]. Thereafter, metastable Ti–5Al–5V–5Mo–3Cr-0.5Fe (Ti-5553) has been commercialised for major die-forging applications on Boeing 787 Dreamliner since the 2000s [11].

A significant increase in ductility and toughness can result from

tailoring phase stability [12,13]. In order to design alloys combining superior mechanical characteristics, the first priority is to understand the microstructure at ambient temperature. When the alloys are cooled rapidly enough from above the  $\beta$ -transus temperature, there is insufficient time for eutectoidal diffusion-controlled decomposition processes to occur, thus the high temperature phase transforms into martensite [14]. For Ti alloys, the high temperature body-centred cubic (bcc)  $\beta$  phase transforms martensitically into a hexagonal close packed (hcp)  $\alpha'$  phase upon quenching, where  $\alpha'$  is crystallographically identical to the equilibrium  $\alpha$  phase. On the other hand, the solid metastable  $\beta$  phase may transform, under external stress, into a distorted hexagonal structure designated  $\alpha''$  which has an orthorhombic unit cell. The  $\alpha''$  phase nucleates heterogeneously as thin laths at existing subgrain boundaries with  $(11\overline{2})_{\beta}//(020)_{\alpha''}$  and  $[1\overline{10}]_{\beta}//[001]_{\alpha''}$  orientation relationships [15]. It may be activated at relatively small strains to accommodate

E-mail address: p.rivera1@lancaster.ac.uk (P.E.J. Rivera-Díaz-del-Castillo).

<sup>\*</sup> Corresponding author.

deformation. The phase stability of Ti alloys can be altered by the addition of  $\beta$ -stabilising elements of two types, isomorphous and eutectoid [4]. In general isomorphous  $\beta$ -stabilisers (such as Mo, V, W, Ta and Nb) decompose to form  $\alpha+\beta$  phases with no intermetallic compounds being formed; however, they are relatively high-cost additions. Conversely, eutectoid  $\beta$ -stabilisers (such as Fe, Cr, Cu and Co) have stronger  $\beta$ -stabilising effects, meaning they are more potent in suppressing the  $\beta$ -transus temperature. Yet a limited addition should be controlled in order to avoid the formation of brittle intermetallics.

The martensitic transformation is characterised by its displacive nature. It may be regarded as a strain transition with shear and dilatational displacements, respectively parallel and normal to the habit plane [16]. Besides, it has been considered a mode of deformation which competes with dislocation slip when external stresses are applied to the parent phase. A thermodynamics-based interpretation of the thermoelastic equilibrium was introduced by Olson and Cohen [17,18] to explain the thermally induced nucleation and growth of thermoelastic martensite. A key parameter indicating the transformation tendency is the martensite start temperature  $M_s$ . For the stress-assisted transition, a pseudoelastic force balance was proposed by Green et al. [19] as a mechanical analogue to the thermoelastic force balance. In addition to the elastic strain energy and the chemical driving force terms, a mechanical work contribution was incorporated to provide the extra transformation driving force for the TRIP effect.

The purpose of this work is threefold. First, an integrated thermoelastic and pseudoelastic modelling approach incorporating thermodynamics and micromechanics is proposed for investigating the energy landscape in  $\beta\!\rightarrow\!\alpha'/\alpha''$  phase transition. The transformational energy barrier, the elastic strain energy and the chemical driving force were quantitatively evaluated; the atomic frictional stress due to solid solution hardening is, for the first time, introduced. Secondly, a series of new alloys are developed by tailoring two widely used commercial Ti alloys: Ti–6Al–4V and Ti–6Al–7Nb. Mo was added in controlled amounts for altering the microstructure and the phase stability [20]. The new alloys are studied by thermodynamic calculations and examined experimentally. Third, the modelling approach was tested via the proposed alloys and the energy landscape for operating transformation-induced plasticity was calculated. It is shown that the composition-dependent threshold value can further guide new alloy design.

### 2. Model development

#### 2.1. Energy barrier for coherent martensitic nuclei

Martensite nucleation upon rapid cooling results from the competition between elastic strain energy and chemical driving force [21]. A martensitic embryo of a given volume will tend to adopt a shape which minimises the combined interfacial and strain energies. In the case of a thin martensite ellipsoidal inclusion with radius a and semi-thickness c, the overall energy barrier associated to the formation of the martensitic particle is [14,17]:

$$\Delta G = 2\pi a^2 \gamma + E_{str} - \Delta G_{chem} \tag{1}$$

where  $\gamma$  is the interfacial energy per unit area of the product phase. The Gibbs free energy change  $\Delta G_{chem} = \Delta g_{chem} \times \frac{4}{3}\pi a^2 c$  and the global stored elastic strain energy  $E_{str} = \Delta g_{str} \times \frac{4}{3}\pi a^2 c$ , where  $\Delta g_{chem}$  is the volumetric chemical driving force [22] and  $\Delta g_{str}$  is the elastic strain energy per unit volume of martensite; therefore Eq. (1) becomes:

$$\Delta G = 2\pi a^2 \gamma + \frac{4}{3}\pi a^2 c (\Delta g_{str} - \Delta g_{chem})$$
 (2)

The elastic strain energy  $\Delta g_{str}$  of the coherent nucleus is more important than the interfacial energy, since the shear component of the pure Bain strain is as high as 0.32 which produces large strains in the surrounding  $\beta$  matrix [14].

#### 2.2. Elastic strain energy & thermoelastic equilibrium

The distortion around a coherent nucleus implies that a crystal containing a product phase is not at its lowest energy state; such extra energy is defined as the nucleus strain energy [23]. The elastic strain energy is computed by defining both martensitic nuclei and  $\beta$  matrix are elastically isotropic. The strain tensor  $\Delta g_{str}$  is divided into deviatoric and hydrostatic components; therefore the coherency strain energy  $\Delta g_{str}^{dila}$  led by a dilatational volume expansion and the transformational strain energy  $\Delta g_{str}^{shear}$  are added to express [21]:

$$\Delta g_{str} = \Delta g_{otr}^{dila} + \Delta g_{otr}^{shear} \tag{3}$$

The elastic strain energy caused by a dilatational volume change comes from Eshelby's elastic field theory of an ellipsoidal inclusion embedded in an infinite elastically isotropic matrix [24]:

$$\Delta g_{str}^{dila} = \frac{2}{9} \frac{(1+\nu)}{(1-\nu)} \left(\frac{\Delta V}{V}\right)^2 \mu \tag{4}$$

where  $\nu$  is the Poisson's ratio,  $\mu$  is the shear modulus which is a function of the absolute temperature T [25].  $\frac{\Delta V}{V}$  is the dilatation and can be expressed by the principal lattice strains [21]:

$$\frac{\Delta V}{V} = \left[\frac{1}{3}(\eta_1 + \eta_2 + \eta_3) + 1\right]^3 - 1\tag{5}$$

where  $\eta_1,\eta_2$  and  $\eta_3$  represent the eigenvalues of the strain tensor; they are evaluated with respect to a Cartesian coordinate system with axes parallel to the orthorhombic unit cells of  $\beta$ ,  $\alpha'$  and  $\alpha''$ , since these axes remain mutually perpendicular upon transformation [26]. Fig. 1 schematically represents each lattice parameter and the atomic displacement in  $\beta\!\rightarrow\!\alpha'$  and  $\beta\!\rightarrow\!\alpha''$  transitions. The principal lattice strains are expressed as [27,28]:

$$\eta_1 = \frac{a_{\alpha}^M - a_{\beta}}{a_{\beta}} \quad \eta_2 = \frac{b_{\alpha}^M - \sqrt{2}a_{\beta}}{\sqrt{2}a_{\beta}} \quad \eta_3 = \frac{c_{\alpha}^M - \sqrt{2}a_{\beta}}{\sqrt{2}a_{\beta}}$$
(6)

where  $a_{\beta}$  is the lattice parameter of the bcc  $\beta$  phase;  $a_{\alpha}^{M}$ ,  $b_{\alpha}^{M}$  and  $c_{\alpha}^{M}$  are the lattice parameter of the martensite, where M designates either hexagonal or orthorhombic phase [29].

On the other hand, the nucleus can form by a simple shear parallel to the plane of the thin ellipsoidal nucleus, and complete coherency is maintained at the interface [14]. Therefore the shape change is approximated by pure shear and is described as [24]:

$$\Delta g_{str}^{shear} = \frac{\pi}{2} \frac{(2-\nu)}{(1-\nu)} \frac{c}{a} s^2 \mu$$
 (7)

where s is the shear component. Therefore the energy barrier  $\Delta G$  associated with the formation of a coherent martensitic nucleus is derived by combining equations above:

$$\Delta G = 2\pi a^2 \gamma + \frac{4}{3}\pi a^2 c \left[ \frac{2}{9} \frac{(1+\nu)}{(1-\nu)} \left( \frac{\Delta V}{V} \right)^2 \mu + \frac{\pi}{2} \frac{(2-\nu)}{(1-\nu)} \frac{c}{a} s^2 \mu - \Delta g_{chem} \right]$$
(8)

The elastic strain energy and interfacial energy oppose the transition, whereas the chemical driving force by Gibbs free energy change promotes it.

Thereafter the thermoelastic force balance can be established. By defining  $T_0$  as the temperature at which the Gibbs free energies of parent and product phases are equal, thus the martensitic nucleation is prohibited above  $T_0$  and the alloy only displays  $\beta$  phase. A martensitic embryo with semi-thickness  $c_0$  and radius  $a_0$  turns into a nucleus as the temperature is below  $T_0$ . Wollants et al. [30] demonstrated that the martensitic embryo grows radially until it hits a barrier such as a high angle grain boundary. The very thin martensitic plates first form with a very large a/c ratio. From that point, the embryo continues to thicken in

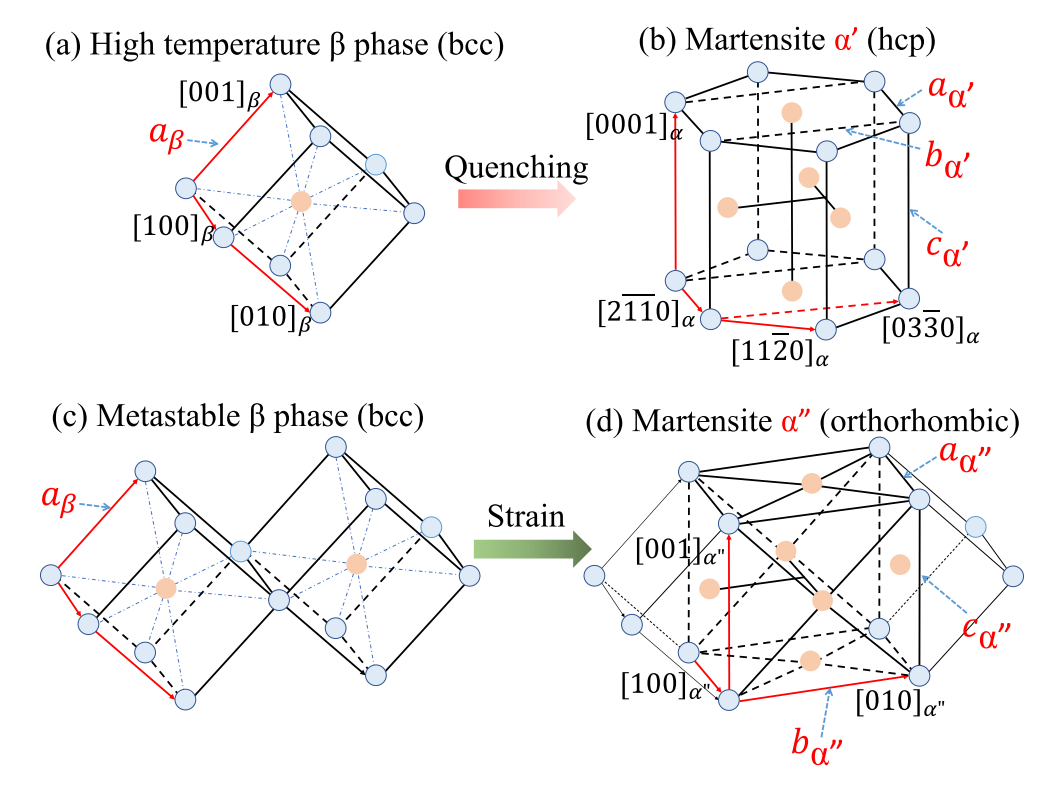


Fig. 1. Schematic representation of the atomic displacement in the  $\beta \rightarrow \alpha'$  transition upon quenching and the  $\beta \rightarrow \alpha''$  transition under external stress. (a) A unit cell of the high temperature bcc  $\beta$  phase; (b) hcp lattice of the  $\alpha'$  martentise; (c) Two unit cell of the room temperature metastable bcc  $\beta$  phase; (d) A unit cell of the orthorhombic  $\alpha''$  martensite.

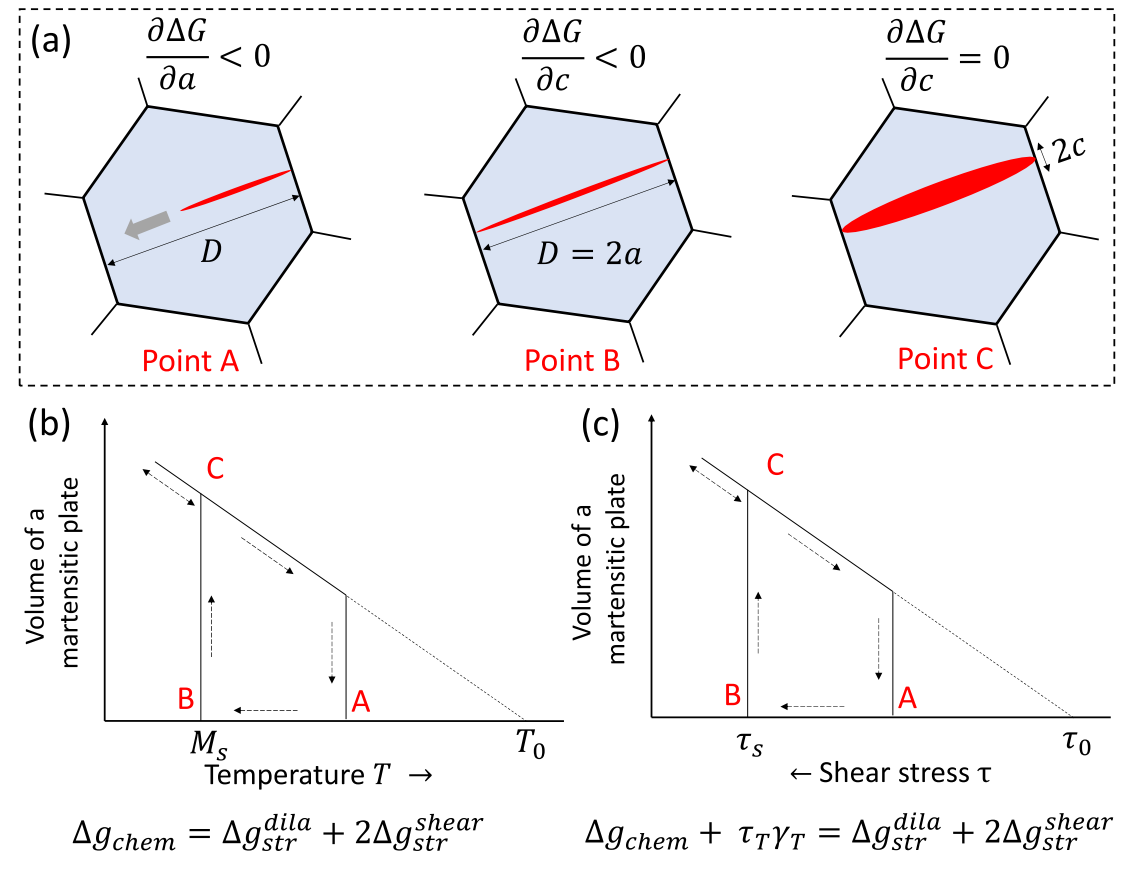


Fig. 2. Schematic representation of (a) the martensite nucleation and growth. The thickening stops when local equilibrium  $(\partial \Delta G/\partial c = 0)$  is reached at the interface between the parent and the product phase. Transformation loops for (b) thermoelasticity and (c) pseudoelasticity. Microstructures corresponding to various points on both loops are depicted in (a).

a direction normal to the plate plane. Following the analysis by Bigon et al. [21], thickening stops until it is arrested as the system energy is depleted ( $\partial \Delta G/\partial c=0$ ) at the interface between the parent and the product phase. Fig. 2a schematically reproduced the nucleation and growth of a nucleus of martensite [21]. The chemical driving force at  $M_s$  is given by differentiating Eq. (8) with respect to c and equating to:

$$\Delta g_{chem}(M_s) = \frac{2}{9} \frac{(1+\nu)}{(1-\nu)} \left(\frac{\Delta V}{V}\right)^2 \mu + \pi \frac{(2-\nu)}{(1-\nu)} \frac{c}{a} s^2 \mu \tag{9}$$

In this case a is the grain radius and c is the minimum detectable semi-thickness of a martensitic plate. Combining with Eqs. (4) and (7), thus Eq. (9) can be written as:

$$\Delta g_{chem} = \Delta g_{str}^{dila} + 2\Delta g_{str}^{shear} \tag{10}$$

This is an ideally reversible thermoelastic force balance at  $M_s$ , where all the transformational strain is accommodated elastically.

#### 2.3. Stress-assisted martensitic transformation

Pseudoelastic force balance refers to the mechanically reversible behaviour commonly observed in thermoelastic martensitic alloys. The addition of an external mechanical work term lowers the transformational energy barrier for pseudoelasticity:

$$\Delta G = 2\pi a^2 \gamma + \frac{4}{3}\pi a^2 c (\Delta g_{str} - \Delta g_{chem} - \tau_T \gamma_T)$$
(11)

where  $\tau_T$  and  $\gamma_T$  is the resolved shear stress and shear strain at the onset of transformation, respectively. A force balance can be derived from an energy expression in Eq. (11) by adopting the lengthening and thickening growth forces in the thermoelastic condition. When the radial growth of a martensitic plate is stopped by obstacles, the plate will continue to thicken in response to the transformational force  $\partial \Delta G/\partial c$  in the c direction. In the absence of frictional resistance, thickening will stop when  $\partial \Delta G/\partial c=0$  and the plate reaches a mechanical equilibrium under the applied stress [19]:

$$\Delta g_{chem} + \tau_T \gamma_T = \Delta g_{str}^{dila} + 2\Delta g_{str}^{shear}$$
 (12)

This equation can be interpreted as follows: thermoelastic-pseudoelastic equilibrium can be achieved when the force generated by the transformational driving free energy is equal to the force generated by the stored elastic strain energy. For thermoelasticity the driving force is  $\Delta g_{chem}$ , whereas for pseudoelasticity this becomes  $\Delta g_{chem} + \tau_{T}\gamma_{T}$ . Fig. 2b and c illustrate an analogy between thermoelastic and pseudoelastic equilibriums. The volume of a single martensitic plate changes as a function of driving force. The driving force for the thermoelastic transformation is inversely proportional to temperature, whereas the driving force for the pseudoelastic transformation at a given temperature increases with applied stress.

The pseudoelastic force balance represents ideal energy balances in plate growth and reversal, i.e. the transformation strain is elastically accommodated and there is no frictional resistance on the transformational interface [19]. A frictional force can be introduced as a reverse stress  $\tau_f$  acting to oppose the dislocation motion. Thus the net driving force for transformation is effectively reduced by the term  $\tau_f \gamma_T$  and the pseudoelastic force balance becomes:

$$\Delta g_{chem} + \tau_T \gamma_T = \Delta g_{str}^{dila} + 2\Delta g_{str}^{shear} + \tau_f \gamma_T$$
 (13)

The frictional resistance term becomes positive when the plate is thickening and negative when it reverts. The internal atomic friction stress  $\tau_f$  is generated by the interactions between dislocations and solutes in the solid solution, where dislocation motions are impeded by such interaction. The stress generated by solid solution hardening (SSH) is [31]:

$$\tau_f = \mu \lambda^{4/3} X_i^{2/3} Z \tag{14}$$

where  $X_i$  is the molar fraction of solute i,  $\lambda$  is a misfit parameter accounting for the solute/solvent lattice parameter misfit and the shear modulus misfit and Z is a temperature-dependent numerical factor whose value can be obtained from a plot of  $d\tau/dX_i^{2/3}$  vs.  $\lambda^{4/3}$ . The detailed SSH calculation was presented in recent work by authors [32]. Here a threshold parameter  $\Delta\Gamma$  is established to describe the energy difference between the transformational promoting terms and the opposing ones:

$$\Delta\Gamma = \Delta g_{chem} + \tau_T \gamma_T - \left(\Delta g_{str}^{dila} + 2\Delta g_{str}^{shear} + \tau_f \gamma_T\right)$$
 (15)

The composition-dependent  $\Delta\Gamma$  defines the energy landscape for pseudoelastic martensitic transition to take place. An equilibrium can be achieved by minimising  $\Delta\Gamma$  such that the chemical driving force  $\Delta g_{chem}$  and mechanical work  $\tau_T \gamma_T$  approach the magnitude of the elastic strain energy  $\Delta g_{str}^{dila} + 2\Delta g_{str}^{shear}$  and the frictional resistant energy  $\tau_T \gamma_T$ . To test the model, a series of alloys were developed and investigated in next sections.

#### 3. Experimental procedure

Commercial Ti64 (Ti-6Al-4V) and Ti67 (Ti-6Al-7Nb) alloy powders supplied by Carpenter Additive were utilised as base materials. The oxygen content in each type of powder is less than 0.06 wt%. Pure Mo powder (99.9 mass %) was added to each grade in controlled amounts for tailoring the microstructure and the phase stability. The alloys were prepared by arc-melting using a nonconsumable tungsten electrode and a water-cooled copper hearth under a Ti gettered argon atmosphere. Each sample with a total mass of 2 g was remelted for 4 times to promote homogeneity and was finally cast into a cylindrical rod with a diameter of 3 mm under a cooling rate of  $\sim 10^3$  K/s [33,34]. Total weight losses during the arc-melting and casting procedure were between 0.05 and 0.10 wt% and the actual O content in each as-cast alloy is less than 0.1 wt%. The compositions of the alloys as well as the corresponding Mo equivalent  $Mo_{eq}$ . [5] are listed in Table 1. In general, a  $Mo_{eq}$  value above of 10 is required to stabilise  $\beta$  phase upon quenching. The two groups of alloys are labelled as Ti64-xMo and Ti67-xMo where x = 10-20, represent the amount of Mo additions. During the rapid cooling, complete solute trapping can be achieved inducing diffusionless solidification [35]. The rapidly solidified alloy systems lead to the supersaturated solid solution with the initial chemical composition of the alloy.

The phase constituents were examined by X-ray diffraction (XRD) with Cu-K $\alpha$  radiation (D8 Advance from Bruker AXS operated at 40 kV and 30 mA equipped with LynxEye detector). XRD line profiles are analysed to evaluate the peak broadening due to the overlapped peaks. Phase analysis was performed by MAUD software on the XRD patterns measured on the cross-sectional flat surface. Compression tests were carried out on a universal testing machine at room temperature under a constant strain rate  $\dot{\epsilon}=5\times 10^{-3}~s_{-1}$ . A strain gauge was used to calibrate and measure the true strain during compression. The tested specimens with a diameter of 3 mm and a length of 6 mm were cut from

Table 1 Compositions of the investigated alloys and their corresponding Mo equivalent values  $Mo_{ea}$ .

. 1			
Alloy label	Composition in mass %	Composition in at.%	$Mo_{eq.}$
Ti64	Ti-6Al-4V	Ti-10.2Al-3.6V	-3.32
Ti64-10Mo	Ti-5.5Al-3.6 V-9Mo	Ti-9.8Al-3.4V-4.5Mo	5.9
Ti64-15Mo	Ti-5.2Al-3.5 V-13Mo	Ti-9.5Al-3.4V-6.7Mo	10.1
Ti64-17Mo	Ti-5.1Al-3.4V-14.5Mo	Ti-9.4Al-3.3V-7.5Mo	11.7
Ti64-20Mo	Ti-5Al-3.3V-16.7Mo	Ti-9.3Al-3.3V-8.7Mo	13.9
Ti67	Ti-6Al-7Nb	Ti-10.5Al-3.6Nb	-4.04
Ti67-10Mo	Ti-5.5Al-6.4Nb-9Mo	Ti-10.1Al-3.4Nb-4.6Mo	5.3
Ti67-15Mo	Ti-5.2Al-6.1Nb-13Mo	Ti-9.8Al-3.3Nb-6.9Mo	9.5
Ti67-18Mo	Ti-5.1Al-5.9Nb-15.3Mo	Ti-9.7Al-3.3Nb-8.2Mo	11.9
Ti67-20Mo	Ti-5Al-5.8Nb-16.7Mo	Ti-9.6Al-3.2Nb-9Mo	13.3

the as-cast rods. Electron backscatter diffraction (EBSD) was performed on a ZEISS Sigma scanning electron microscope (SEM). Bruker QUANTAX software was used to acquire and post-process data. The cross-sectional microstructure were characterised comparatively to reveal the formation of deformation bands at 10% strain. The equilibrium phase fraction vs. temperature during bcc to hcp transition in each alloy was calculated by Thermo-Calc using TCTI1:Ti-Alloys thermodynamic database.

#### 4. Experimental data

An essential ingredient of the alloy design effort is an accurate description of thermodynamic properties within the composition design space. Fig. 3 displays the equilibrium diagrams of the Ti64-xMo and Ti67-xMo alloys, revealing a change in phase fraction with cooling temperature. Increasing the Mo content leads to a wider temperature widow for the high temperature bcc phase, which further delays the formation of hcp phase and stabilises  $\beta$  phase at ambient temperature. Fig. 4 exhibits the variation of Gibbs free energy in bcc and hcp phases as a function of Mo content at room temperature. The chemical driving force for the transition can be obtained from  $\Delta G^{bcc \rightarrow hcp} = G^{bcc} - G^{hcp}$ . The value of  $\Delta G^{bcc \to hcp}$  decreases with the addition of Mo, suggesting the transition is inhibited. The intersection of the two curves represents the composition where the chemical driving force vanishes; alloys with  $\Delta G^{bcc \to hcp} < 0$  display a  $\beta$  phase fully stabilised at ambient temperature. A quantitative interpretation on the Gibbs free energy change is presented in Section 5.

Fig. 5 shows the XRD phase constituents of the investigated alloys. Both Ti64 and Ti67 base alloys exhibited strong martensitic  $\alpha'$  phase without visible  $\beta$ -peaks from the diffraction patterns (Fig. 5a). The supersaturated  $\beta$  solid solution become more prominent whilst increasing the Mo additions (Fig. 5b and d). Full  $\beta$  phase was retained in high Mo containing alloys such as Ti64–15Mo, Ti64–20Mo, Ti67–18Mo and Ti67–20Mo. It is widely acknowledged that bcc to orthorhombic

martensitic transformation occurs under deformation, whereas bcc to hcp transition happens upon rapid cooling. In the exceptional cases that hcp  $\alpha'$  forms from the bcc matrix under external stress,  $\alpha'$  can only be triggered in alloy compositions of very low phase stability – even fully  $\beta$  phase cannot be retained at ambient temperature and the microstructure contains primary  $\alpha$  phase from quenching [36]. Besides more evidence would be required to prove that  $\alpha'$  phase does transform from the  $\beta$  phase. This means  $\alpha''$  is the only strain-induced transformation product commonly forming in the present type of metastable Ti alloy, which is well identified in literature [21,37]. A broadening of the main  $\beta$  (110) peak was observed in Ti67–18Mo upon deformation till failure. Peak analysis (Fig. 5f) identified it consists of orthorhombic  $\alpha''$  (002) peak, suggesting  $\beta \rightarrow \alpha''$  transition was activated upon deformation in Ti67–18Mo.

Fig. 6 displays the true stress-strain curves of the Ti64-xMo and Ti67-xMo alloys. The alloys (Ti64 and Ti67) consisting of larger amount of  $\alpha'$  phases exhibit superior yield stress but limited plasticity compared to single  $\beta$  systems. The high yield stress mainly stems from the hard  $\alpha'$ , yet  $\alpha'$  displays lower ductility due to a limited number of slip systems of the hcp lattice. The yield stress decreased with the addition of Mo from Ti64 to Ti64–15Mo alloy where larger a fraction of  $\beta$  phase was retained. Thereafter, the yield stress increases again from Ti64–15Mo to Ti64–20Mo alloy due to the enhanced solid solution strengthening; concomitantly the  $\beta$  alloys exhibited superior ductility. Similar trends were found in the Ti67-xMo series alloys.

Fig. 7 exhibits the deformation microstructures of the selected Ti64–10Mo and Ti67–18Mo alloys upon 10% strain. The SEM back-scattered electron image of Ti64–10Mo (Fig. 7a) displays parallel slip bands in the  $\beta$  grains and with their propagation being obstructed by grain boundaries. The EBSD pattern quality maps of Ti64–10Mo (Fig. 7b) and Ti67–18Mo (Fig. 7c) clearly identified the grain boundaries as well as the formation of shear bands. Some of the shear bands are thickened to accommodate the inhomogeneously distributed strain

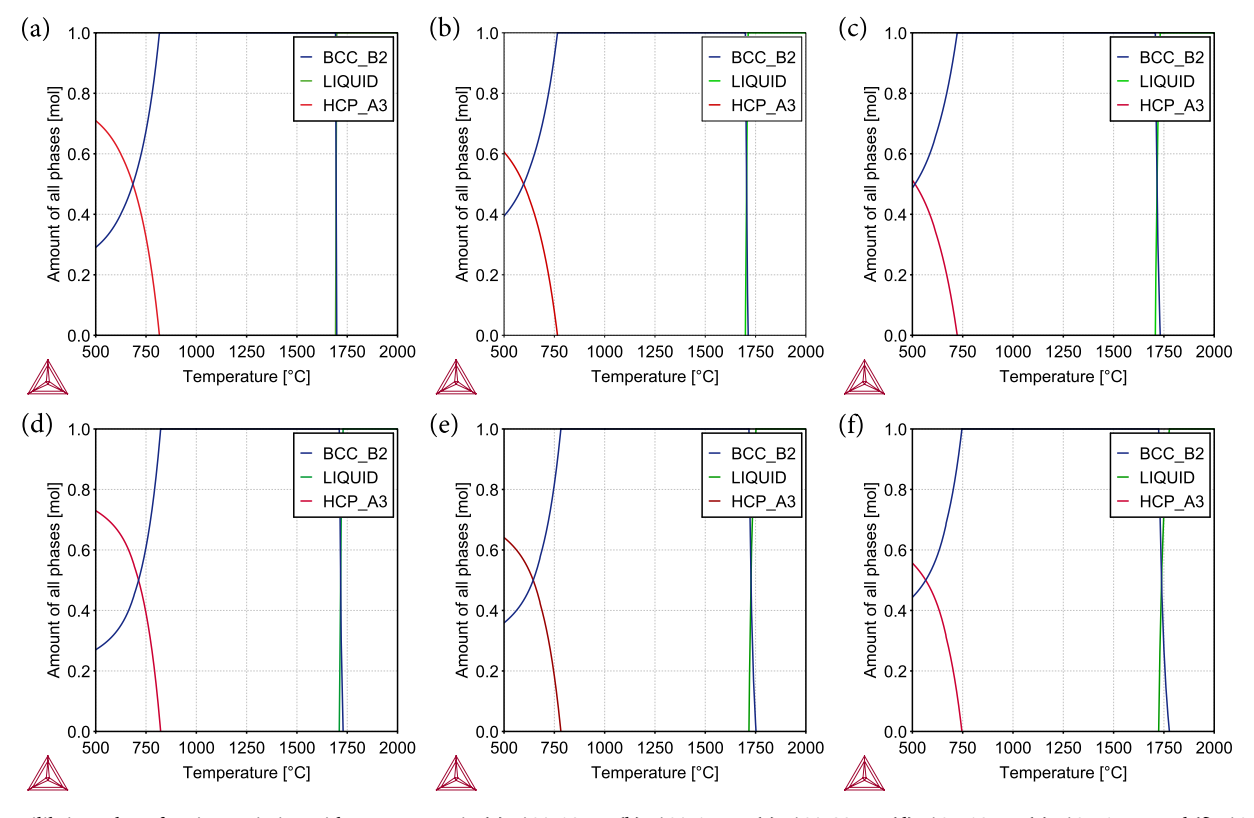


Fig. 3. Equilibrium phase fraction variation with temperature in (a) Ti64–10Mo, (b) Ti64–15Mo, (c) Ti64–20Mo, (d) Ti67–10Mo, (e) Ti67–15Mo and (f) Ti67–20Mo. The calculation was performed by using the Thermo-Calc database TCTI1: Ti-Alloys.

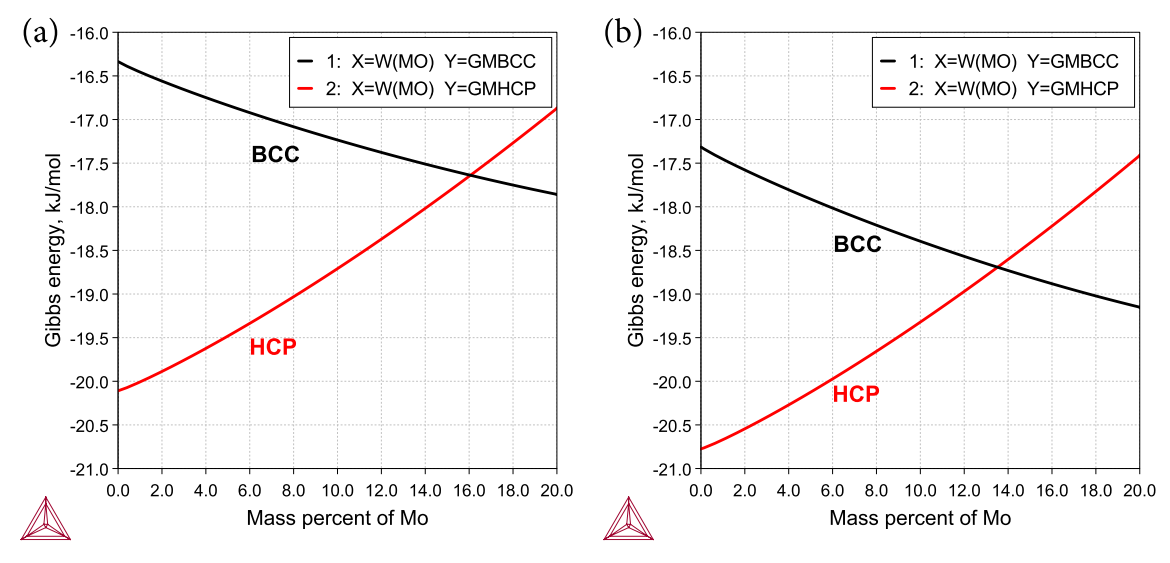


Fig. 4. The Gibbs free energy changes of the bcc and hcp phases as a function of Mo contents in (a) Ti64-xMo and (b) Ti67-xMo alloys at room temperature.

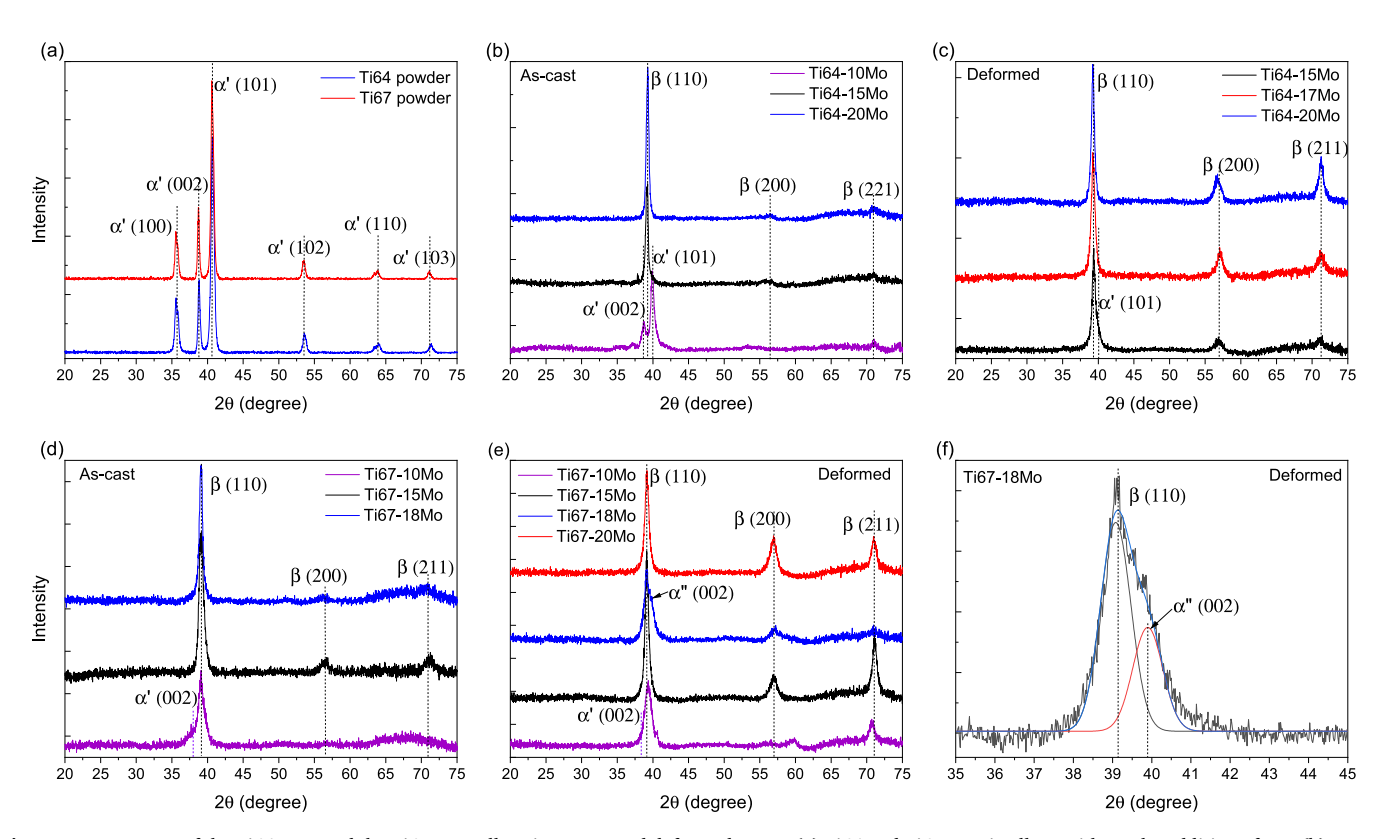
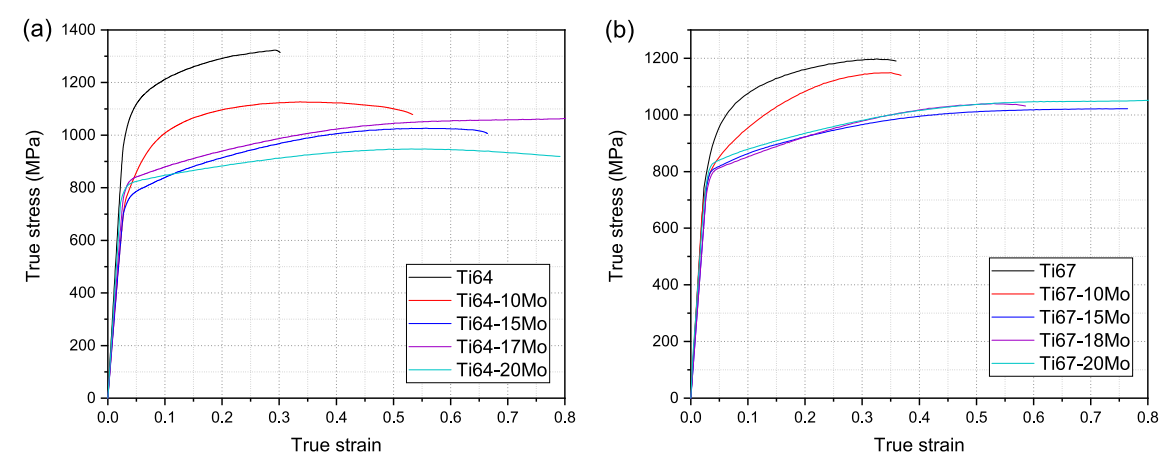


Fig. 5. XRD patterns of the Ti64-xMo and the Ti67-xMo alloys in as-cast and deformed states: (a) Ti64 and Ti67 matrix alloys without the addition of Mo; (b) as-cast Ti64-xMo alloys, (c) deformed Ti67-xMo alloys, (d) as-cast Ti67-xMo alloys, (e) deformed Ti67-xMo alloys and (f) peak analysis of the deformed Ti67-18Mo alloy showing the formation of strain-induced  $\alpha''$  phase.

[38]. Although extensive deformation bands were observed, no trace of mechanical twinning was observed in neither alloy. According to our previous work [39], the significant strain-hardening observed in TWIP and TRIP/TWIP Ti alloys mainly stems from the reduced dislocation mean free path cut by the dynamic activation of mechanical twinning, as well as from the kinematic hardening due to the enhanced dislocation pile-up at coherent twin interfaces. The absence of twinning brought moderate strain-hardening, even though strain-induced martensitic transformation was operated. Besides, the role of martensite on strain-hardening is still controversial, as it is classically considered as a soft phase with a modulus lower than that of  $\beta$  matrix; and recent studies

reflect orthorhombic martensites may provide relatively limited strain-hardening as they act as less effective obstacles for dislocation glide [37,40].

Fig. 8 presents the phase stability map of Ti alloys by accounting for the composition-dependent electronic structures [41]. Bond order Bo exhibits the electron cloud overlap between solute and solvent, which is a measurement of the covalent bond strength between the alloying elements and the matrix. Metal d-orbital energy level Md correlates with the electronegativity and atomic radii of the solutes. The electronic parameters of each element were calculated by means of the molecular orbital method [42,43]. The average  $\overline{Bo}$  and  $\overline{Md}$  value of each alloy are



**Fig. 6.** Mechanical properties of the (a) Ti64-xMo and (b) Ti67-xMo alloys at room temperature. The base alloys with large fractions of  $\alpha'$  phase showed higher yield stress but limited ductility, whereas the  $\beta$  alloys presented excellent plasticity via strain-hardening.

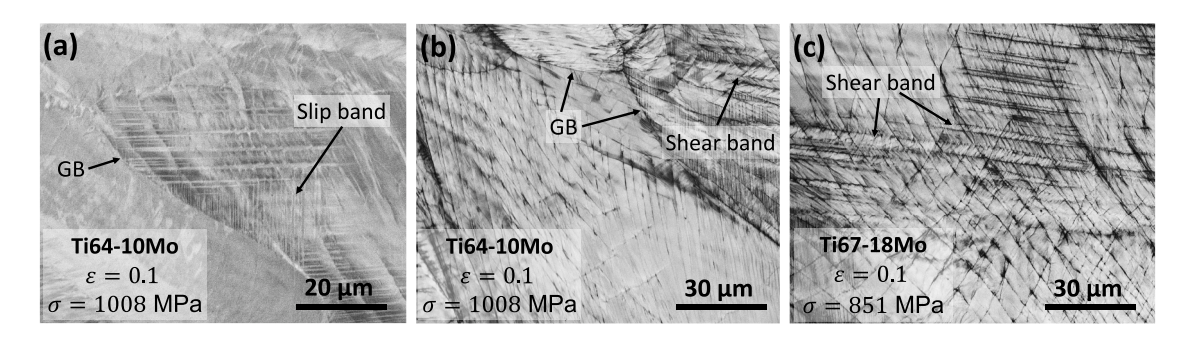
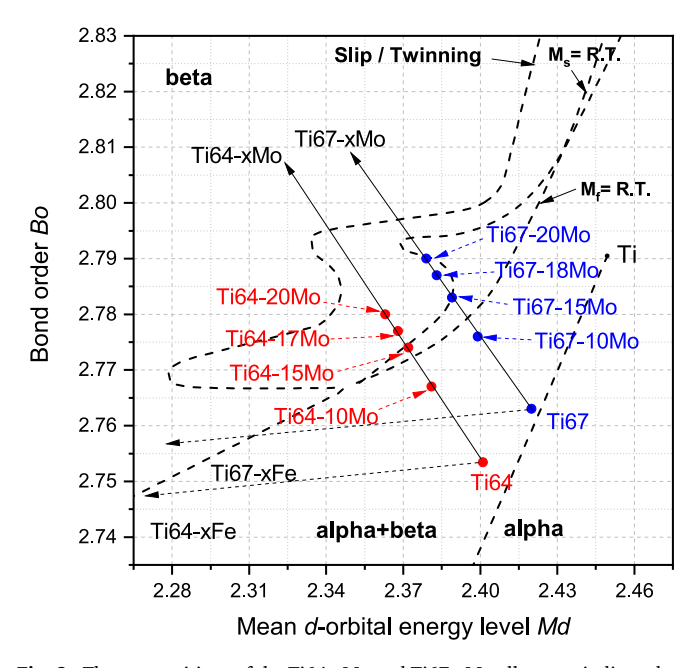


Fig. 7. Deformation microstructures of the selected Ti64–10Mo and Ti67–18Mo alloys upon 10% strain. (a) SEM backscattered electron (BSE) image of Ti64–10Mo alloy showing extensive interactions of deformation bands; EBSD pattern quality map of (b) Ti64–10Mo and (c) Ti67–18Mo, respectively.



**Fig. 8.** The compositions of the Ti64-xMo and Ti67-xMo alloys are indicated on the phase stability map. The alloy locations transit from the  $\alpha+\beta$  region to the metastable  $\beta$  region as the increase of Mo contents. In contrast, the vectors of Ti64-xFe and Ti67-xFe alloys directly lead to the stabilised  $\beta$  region.

simply computed by the compositional average:  $\overline{Bo} = \sum (Bo)_i X_i$  and  $\overline{Md} = \sum (Md)_i X_i$ . Dash borders divide  $\alpha$ ,  $\alpha + \beta$  and  $\beta$  phase domains, as well as to aid in distinguishing deformation modes [41]. The Ti64-xMo and Ti67-xMo vectors transited from the  $\alpha + \beta$  domain to the metastable  $\beta$  domain with the increasing of Mo, implying the metastable alloys are likely to trigger TRIP/TWIP effects upon deformation. Nevertheless, one has to keep in mind that the dividing borders were illustrated empirically from early experimental data so that many modern TRIP/TWIP alloys violate the boundary constrains [39], meaning it may not play a determinant role in predicting the operative deformation mechanisms. Preferably the alloying vectors may provide a visual aid to reflect the effects of different stabilising elements on the transition between deformation modes.

#### 5. Model application & discussion

The model integrating pseudoelasticity arising from stress-assisted martensitic transformation, is applied to the Ti64-xMo and Ti67-xMo alloys. Volumetric chemical driving force can be obtained from  $\Delta g_{chem} = \Delta G_{chem}/V_m^{\varphi}$ , where  $\Delta G_{chem}$  is the molar Gibbs energy difference between the parent and the product phases. The values were obtained from TCTI1:Ti-Alloys thermodynamic database and listed in Table 2.  $V_m^{\varphi}$  is the molar volume of phase  $\varphi$  and its value can be calculated by a linear combination of pure elements plus a regular-solution model for the excess volume [44]:

$$V_m^{\varphi} = \sum_i X_i V_{m,i}^{\varphi} + \sum_{i < j} X_i X_j \Omega_{i,j}^{\varphi}$$
(16)

where  $X_i$  denotes the molar fraction of element i and here  $X_j$  denotes the

Table 2
The Gibbs free energy difference  $\Delta G_{chem}$  and volumetric chemical driving force  $\Delta g_{chem} = \Delta G_{chem}/V_m$  in each alloy at room temperature. The energy contributions from external stress  $\tau$  and internal frictional stress  $\tau_f$ , as well as from dilatation  $\frac{\Delta V}{V}$ ; the corresponding coherent strain energy  $\Delta g_{str}^{dila}$ , the minimum total strain energy term  $\Delta g_{str}^{dila} + 2\Delta g_{str}^{shear}$  and the introduced energy difference parameter  $\Delta \Gamma$  in each alloy are listed.

Alloy	$\Delta G_{chem}(\mathrm{J/mol})$	$\Delta g_{chem}(\times 10^7 \text{ J/m}_3)$	$\frac{\Delta V}{V}$ ( $ imes 10^{-3}$ )	$\Delta g_{str}^{dila}(\times 10^7 \text{ J/m}_3)$	$\Delta g_{str}^{dila} + 2\Delta g_{str}^{shear} ( imes 10^7  ext{ J/m}_3)$	$\tau_f \gamma_T (\times 10^7 \text{ J/m}_3)$	ΔΓ(J/mol)
Ti64	+3488	33.63	1.4	$0.003\pm0.001$	$3.82 \pm 0.08$	1.60	$4166\pm265$
Ti64-10Mo	+1690	16.41	9	$0.14\pm 0.05$	$3.95 \pm 0.12$	1.99	$2176\pm183$
Ti64-15Mo	+756	7.38	14.2	$0.35\pm 0.08$	$4.16 \pm 0.16$	2.18	$1072\pm166$
Ti64-17Mo	+318	3.11	16.0	$0.44 \pm 0.12$	$4.26\pm0.19$	2.23	$705\pm128$
Ti64-20Mo	-206	-2.02	18.9	$0.62 \pm 0.15$	$4.43 \pm 0.21$	2.33	$237 \pm 98$
Ti67	+3458	33.02	1.5	$\boldsymbol{0.004 \pm 0.002}$	$3.82 \pm 0.09$	0.82	$4067 \pm 258$
Ti67-10Mo	+1226	11.82	11.9	$\boldsymbol{0.24 \pm 0.06}$	$4.06\pm0.13$	1.38	$1723\pm178$
Ti67-15Mo	+128	1.26	17.2	$0.51 \pm 0.10$	$4.32 \pm 0.19$	1.61	$559\pm139$
Ti67-18Mo	-272	-2.64	20.3	$0.71 \pm 0.13$	$4.52 \pm 0.26$	1.74	$123 \pm 96$
Ti67-20Mo	-678	-6.60	22.0	$0.83\pm 0.18$	$4.65\pm0.29$	1.81	$279 \pm 118$

molar fraction of Ti solvent.  $\Omega_{ij}^{\varphi}$  is the molar volume interaction parameter between each solute and the Ti solvent [44]. Applying the compositions of Ti64-xMo and Ti67-xMo alloys to Eq. (16), the calculated mean molar volume is  $1.02\times 10^{-5}$  and  $1.03\times 10^{-5}$  m<sub>3</sub>/mol, respectively. The volume dilatation of the  $\beta\!\rightarrow\!\alpha'/\alpha''$  martensitic transformation can be calculated using the current molar-volume assessment [44]:

$$\frac{\Delta V}{V} = \frac{V_m^{\alpha'/\alpha''} - V_m^{\beta}}{V_m^{\beta''}} \tag{17}$$

The dilatational strain energy  $\Delta g_{str}^{dila}=\frac{2}{9}\frac{(1+\nu)}{(1-\nu)}\left(\frac{\Delta V}{V}\right)^2\mu$  is obtained by the composition-dependent dilatation  $\frac{\Delta V}{V}$ .  $\nu\approx 0.33$  is the Poisson's ratio and  $\mu=39$  GPa the shear modulus of the Ti alloys at room temperature [45].

The transformational strain energy  $\Delta g_{str}^{shear} = \frac{\pi}{2} \frac{(2-\nu)}{(1-\nu)} \frac{c}{a} s^2 \mu$  can be calculated in the following manner.  $\beta \rightarrow \alpha''$  transition is associated with the  $\{332\}\langle113\rangle$  twinning [46,47], which is unique as the most operative twinning system in metastable Ti alloys. A fundamental crystallographic model [48] suggests {332}(113) twinning only moves one-half of the atoms from the untwinned lattice sites with an associated shear strain  $\frac{1}{2\sqrt{2}}$ , then additional shuffling is necessary to transport the rest atoms. Therefore the transformational shear equals to the corresponding shear strain produced by  $\{332\}\langle 113\rangle$  twinning with  $s=\gamma_{\{332\}\langle 113\rangle}=\frac{1}{2\sqrt{2}}$ . The detectable semi-thickness of a martensitic plate by transmission electron microscopy is c = 50 nm [49]. The average grain size of the samples was 100  $\mu$ m, thus  $a = 50 \mu$ m. Combining the data above, the shear-induced strain energy  $\Delta g_{str}^{\textit{shear}} = 1.91 \times 10^7$  J/m3. Note that calculated  $\Delta g_{str}^{\textit{dila}} +$  $2\Delta g_{str}^{shear}$  should be a minimum value, since the c/a ratio increases as the martensitic plate grows. The fact that these nuclei remained after stress release implies that the elastic strain energy was reduced via plastic accommodation [19], which prevented their complete reversion. Referring to the critical resolved shear stress  $\tau_T$  to active transformation, such term can be obtained from the experimental stress-strain curves.  $\tau_T$ is taken as the resolved yield stress corresponding to the first plates to form, where multiple-plate interactions would be minimal [50]. The composition-dependent internal frictional stress  $\tau_f$  was interpreted by the solid solution hardening  $\tau_f = \mu \lambda^{4/3} X_i^{2/3} Z$ .

The values of each component in  $\Delta\Gamma=\Delta g_{chem}+\tau_T\gamma_T-(\Delta g_{str}^{dila}+2\Delta g_{str}^{shear}+\tau_f\gamma_T)$  are listed in Table 2. The transformational energy landscape  $\Delta\Gamma$  vs. molar chemical driving force is illustrated in Fig. 9.  $\beta\to\alpha'/\alpha''$  transition is operative when  $\Delta\Gamma\geqslant 0$ , since the energy promoting phase transformation is larger than the opposing term.  $\Delta\Gamma$  decreases as the addition of  $\beta$ -stabilisers, which is associated

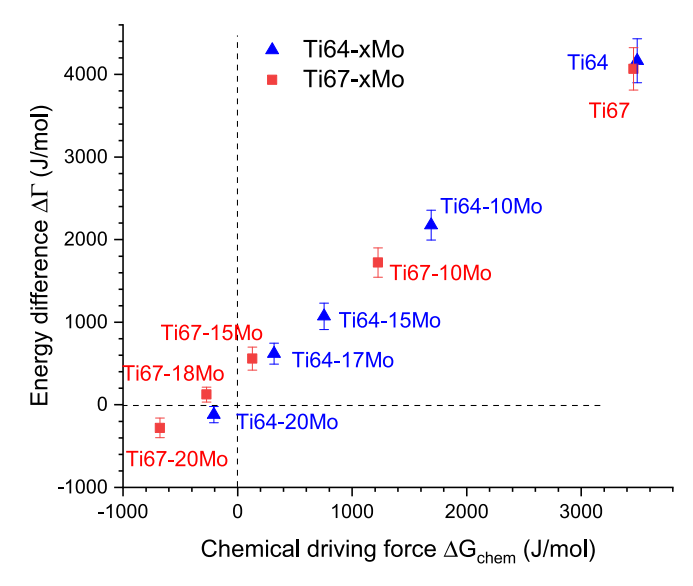


**Fig. 9.** The transformational energy landscape  $\Delta\Gamma vs.$  chemical driving force  $\Delta G_{chem}$  in each alloy. The positive energy difference  $\Delta\Gamma$  moving towards to 0 as the decreasing of  $\Delta G_{chem}$ , meaning that pseudoelastic force balance becomes achievable within appropriate energy domain.

with the considerably reduced chemical driving force. The positive  $\Delta\Gamma$  moving towards to 0 as the decreasing of  $\Delta G_{chem}$ , meaning that pseudoelastic force balance becomes achievable within appropriate energy threshold. The  $\Delta\Gamma$  of Ti67–18Mo alloy is the positively closest towards 0 so that pseudoelastic equilibrium is comparatively favoured. Other alloys become stabilised at ambient temperature as fully  $\beta$  phase when  $\Delta\Gamma<0$ , where martensitic transformation can hardly take place.

The current model treat the orthorhombic  $\alpha''$  martensite and the hcp  $\alpha'$  phase energetically equivalent in thermodynamic calculations. It is reasonable to describe the  $\beta\!-\!\alpha''$  transformation as a crystallographically incomplete  $\beta\!-\!\alpha'$  transformation that should have a similar transformation enthalpy change, given by orthorhombic martensite has a crystal structure intermediate between bcc and hcp lattices [1]. The integrated model was quantitatively tested by experimental data, which adopt composition-dependent input such as the chemical driving force, the lattice dilatation and the elastic strain energy. The frictional resistance was interpreted by the effect of solid solution hardening, where atomic friction was generated by the interactions between the mobile dislocations and the solute atoms. The energy landscape by the calculations can be employed as a criterion to guide plasticity-oriented Ti alloy design.

#### 6. Conclusions

An integrated thermoelastic and pseudoelastic model was built to evaluate  $\beta$  stability and phase transformations in Ti alloys. The model explicitly calculated the energy landscape to operate  $\beta \rightarrow \alpha'/\alpha''$  transition, where the competition between chemical driving force and elastic strain energy dominates the transformation equilibrium. Two commercial Ti alloys, Ti64 and Ti67, were tailored with various Mo additions to test the model. The alloys with fully retained  $\beta$  phase exhibited superior ductility, where strain-induced orthorhombic  $\alpha''$  martensite was found in Ti67-18Mo alloy. The formation of martensite may accommodate strain yet the contribution to strain-hardening is relatively moderate with the absence of deformation twinning. A composition-dependent phase stability parameter  $\Delta\Gamma$  was proposed to define the energy threshold for transformation-induced plasticity. Martensitic transitions perform when  $\Delta\Gamma \geqslant 0$ , since the promoting energy is larger than the opposing term.  $\Delta\Gamma$  decreases as the addition of  $\beta$ -stabilisers, which is associated with the considerably reduced chemical driving force. The alloy preserves relatively stabilised  $\beta$  phase at ambient temperature when  $\Delta\Gamma$  < 0, where martensitic transition is not operative neither upon cooling nor under external stress. A comprehensive modelling approach incorporating thermodynamics and micromechanics is presented; this can be applied to alloy design and to predict strain-induced martensitic transformation in metastable alloys.

#### Data availability

The data that support the findings of this study are available upon reasonable request.

#### CRediT authorship contribution statement

G.-H. Zhao: Performed conceptualisation, computation, Formal analysis, Manuscript writing and reviewing. X.Z. Liang: Methodology, Performed mechanical testing and aided in methodology. X. Xu: EBSD analysis and interpretation of associated data. M.B. Gamža: Performed experimental casts and X-ray analysis, supporting overall methodology. H. Mao: Thermodynamic analysis, modelling and interpretation of data. D.V. Louzguine-Luzgin: Thermodynamic analysis, modelling and interpretation of data. P.E.J. Rivera-Díaz-del-Castillo: Conceptualization, Writing — original draft, Supervision, Funding acquisition, Manuscript writing and reviewing, conceptualisation, supervision and funding acquisition.

#### Declaration of competing interest

The authors declare that they have no known competing financial interests or personal relationships that could have appeared to influence the work reported in this paper.

### Acknowledgements

This work is supported by Designing Alloys for Resource Efficiency (DARE) grant EP/L025213/1 from the UK Engineering and Physical Science Research Council (EPSRC). PEJRDC is grateful to the Royal Academy of Engineering for Chair sponsorship via grant RCSRF1718/5/32.

#### References

- J.-Y. Yan, G.B. Olson, Computational thermodynamics and kinetics of displacive transformations in titanium-based alloys, J. Alloys Compd. 673 (2016) 441–454.
- [2] W. Xu, K. Kim, J. Das, M. Calin, J. Eckert, Phase stability and its effect on the deformation behavior of Ti–Nb–Ta–In/Cr β alloys, Scripta Mater. 54 (11) (2006) 1943–1948.

- [3] H. Kim, Y. Ikehara, J. Kim, H. Hosoda, S. Miyazaki, Martensitic transformation, shape memory effect and superelasticity of Ti–Nb binary alloys, Acta Mater. 54 (9) (2006) 2419–2429.
- [4] P.J. Bania, Beta titanium alloys and their role in the titanium industry, JOM 46 (7) (1994) 16–19.
- [5] R.P. Kolli, W.J. Joost, S. Ankem, Phase stability and stress-induced transformations in beta titanium alloys, JOM 67 (6) (2015) 1273–1280.
- [6] G.-H. Zhao, S.V. Ketov, H. Mao, A. Borgenstam, D.V. Louzguine-Luzgin, Ti-Fe-Sn-Nb hypoeutectic alloys with superb yield strength and significant strain-hardening, Scripta Mater. 135 (2017) 59–62.
- [7] T.M. Pollock, Alloy design for aircraft engines, Nat. Mater. 15 (8) (2016) 809.
- [8] P. Castany, T. Gloriant, F. Sun, F. Prima, Design of strain-transformable titanium alloys, C.R. Phys. 19 (8) (2018) 710–720.
- [9] R.R. Boyer, Aerospace applications of beta titanium alloys, JOM 46 (7) (1994) 20–23
- [10] R.R. Boyer, An overview on the use of titanium in the aerospace industry, Mater. Sci. Eng. A 213 (1–2) (1996) 103–114.
- [11] J.D. Cotton, R.D. Briggs, R.R. Boyer, S. Tamirisakandala, P. Russo, N. Shchetnikov, J.C. Fanning, State of the art in beta titanium alloys for airframe applications, JOM 67 (6) (2015) 1281–1303.
- [12] G. Carter, H. Flower, G. Pennock, D. West, The deformation characteristics of metastable β-phase in a Ti-15 wt% Mo alloy, J. Mater. Sci. 12 (11) (1977) 2149–2153.
- [13] K. Lu, Stabilizing nanostructures in metals using grain and twin boundary architectures, Nat. Rev. Mater. 1 (5) (2016) 1–13.
- [14] D.A. Porter, K.E. Easterling, M. Sherif, Phase Transformations in Metals and Alloys, (Revised Reprint), CRC Press, 2009.
- [15] L. Zhang, T. Zhou, M. Aindow, S. Alpay, M. Blackburn, M. Wu, Nucleation of stress-induced martensites in a Ti/Mo-based alloy, J. Mater. Sci. 40 (11) (2005) 2833–2836.
- [16] J. Patel, M. Cohen, Criterion for the action of applied stress in the martensitic transformation, Acta Metall. 1 (5) (1953) 531–538.
- [17] G. Olson, M. Cohen, Thermoelastic behavior in martensitic transformations, Scripta Metall. 9 (11) (1975) 1247–1254.
- [18] G. Olson, M. Cohen, Reply to "On the equilibrium temperature in thermoelastic martensitic transformations", Scripta Metall. 11 (5) (1977) 345–347.
- [19] M.L. Green, M. Cohen, G. Olson, The pseudoelastic force balance and its application to β-Fe-Be alloys, Mater. Sci. Eng., A 50 (1) (1981) 109–116.
- [20] B. Vrancken, L. Thijs, J.-P. Kruth, J. Van Humbeeck, Microstructure and mechanical properties of a novel β titanium metallic composite by selective laser melting. Acta Mater. 68 (2014) 150–158.
- [21] M. Bignon, E. Bertrand, F. Tancret, P.E.J. Rivera-Díaz-del-Castillo, Modelling martensitic transformation in titanium alloys: the influence of temperature and deformation, Materialia 7 (2019) 100382.
- [22] T.M. Pollock, A. Van der Ven, The evolving landscape for alloy design, MRS Bull. 44 (4) (2019) 238–246.
- [23] D. Hull, D.J. Bacon, Introduction to Dislocations, Butterworth-Heinemann, 2001.
- [24] J.D. Eshelby, The determination of the elastic field of an ellipsoidal inclusion, and related problems, Proc. R. Soc. A: Math. Phys. Eng. Sci. 241 (1226) (1957) 376–396.
- [25] E.I. Galindo-Nava, On the prediction of martensite formation in metals, Scripta Mater. 138 (2017) 6–11.
- [26] M. Bönisch, M. Calin, L. Giebeler, A. Helth, A. Gebert, W. Skrotzki, J. Eckert, Composition-dependent magnitude of atomic shuffles in Ti–Nb martensites, J. Appl. Crystallogr. 47 (4) (2014) 1374–1379.
- [27] M. Bönisch, T. Waitz, M. Calin, W. Skrotzki, J. Eckert, Tailoring the Bain strain of martensitic transformations in Ti-Nb alloys by controlling the Nb content, Int. J. Plast. 85 (2016) 190–202.
- [28] T. Inamura, J. Kim, H. Kim, H. Hosoda, K. Wakashima, S. Miyazaki, Composition dependent crystallography of α-martensite in Ti–Nb-based β-titanium alloy, Philos. Mag. A 87 (23) (2007) 3325–3350.
- [29] X. Ji, I. Gutierrez-Urrutia, S. Emura, T. Liu, T. Hara, X. Min, D. Ping, K. Tsuchiya, Twinning behavior of orthorhombic-α" martensite in a Ti-7.5Mo alloy, Sci. Technol. Adv. Mater. 20 (1) (2019) 401–411.
- [30] P. Wollants, J. Roos, L. Delaey, Thermally- and stress-induced thermoelastic martensitic transformations in the reference frame of equilibrium thermodynamics, Prog. Mater. Sci. 37 (1993) 227–288.
- [31] R.E. Smallman, R.J. Bishop, Modern Physical Metallurgy and Materials Engineering, elsevier, 1999.
- [32] G.-H. Zhao, X. Liang, B. Kim, P.E.J. Rivera-Díaz-del-Castillo, Modelling strengthening mechanisms in beta-type Ti alloys, Mater. Sci. Eng. A 756 (2019) 156–160.
- [33] D. Louzguine-Luzgin, G. Xie, Q. Zhang, C. Suryanarayana, A. Inoue, Formation, structure, and crystallization behavior of Cu-based bulk glass-forming alloys, Metall. Mater. Trans. 41 (7) (2010) 1664–1669.
- [34] G.-H. Zhao, H. Mao, D.V. Louzguine-Luzgin, Glass forming range of the Ti-Fe-Si amorphous alloys: an effective materials-design approach coupling calphad and topological instability criterion, J. Appl. Phys. 120 (20) (2016) 205106.
- [35] P. Galenko, Solute trapping and diffusionless solidification in a binary system, Phys. Rev. E 76 (3) (2007), 031606.
- [36] S. Lee, C. Park, J. Hong, J.-t. Yeom, The role of nano-domains in {1–011} twinned martensite in metastable titanium alloys, Sci. Rep. 8 (1) (2018) 1–9.
- [37] L. Lilensten, Y. Danard, C. Brozek, S. Mantri, P. Castany, T. Gloriant, P. Vermaut, F. Sun, R. Banerjee, F. Prima, On the heterogeneous nature of deformation in a strain-transformable beta metastable Ti-V-Cr-Al alloy, Acta Mater. 162 (2019) 268–276.

- [38] G. Miyamoto, A. Shibata, T. Maki, T. Furuhara, Precise measurement of strain accommodation in austenite matrix surrounding martensite in ferrous alloys by electron backscatter diffraction analysis, Acta Mater. 57 (4) (2009) 1120–1131.
- [39] G.-H. Zhao, X. Xu, D. Dye, P.E.J. Rivera-Díaz-del-Castillo, Microstructural evolution and strain-hardening in TWIP Ti alloys, Acta Mater. 183 (2020) 155–164.
- [40] M. Lai, T. Li, D. Raabe,  $\omega$  phase acts as a switch between dislocation channeling and joint twinning-and transformation-induced plasticity in a metastable  $\beta$  titanium alloy, Acta Mater. 151 (2018) 67–77.
- [41] D. Kuroda, M. Niinomi, M. Morinaga, Y. Kato, T. Yashiro, Design and mechanical properties of new β-type titanium alloys for implant materials, Mater. Sci. Eng. A 243 (1–2) (1998) 244–249.
- [42] M. Morinaga, Alloy design based on molecular orbital method, Mater. Trans. (2016), M2015418.
- [43] M. Abdel-Hady, K. Hinoshita, M. Morinaga, General approach to phase stability and elastic properties of β-type Ti-alloys using electronic parameters, Scripta Mater. 55 (5) (2006) 477–480.

- [44] J.-Y. Yan, G.B. Olson, Molar volumes of bcc, hcp, and orthorhombic Ti-base solid solutions at room temperature, Calphad 52 (2016) 152–158.
- [45] G.-H. Zhao, S.V. Ketov, J. Jiang, H. Mao, A. Borgenstam, D.V. Louzguine-Luzgin, New beta-type Ti-Fe-Sn-Nb alloys with superior mechanical strength, Mater. Sci. Eng. A 705 (2017) 348–351.
- [46] M. Lai, C.C. Tasan, D. Raabe, On the mechanism of {332} twinning in metastable  $\beta$  titanium alloys, Acta Mater. 111 (2016) 173–186.
- [47] K. Cho, R. Morioka, S. Harjo, T. Kawasaki, H.Y. Yasuda, Study on formation mechanism of {332}<113> deformation twinning in metastable β-type Ti alloy focusing on stress-induced α" martensite phase, Scripta Mater. 177 (2020) 106–111.
- [48] A. Crocker, Twinned martensite, Acta Metall. 10 (2) (1962) 113-122.
- [49] W. Zhu, J. Lei, C. Tan, Q. Sun, W. Chen, L. Xiao, J. Sun, A novel high-strength  $\beta$ -Ti alloy with hierarchical distribution of  $\alpha$ -phase: the superior combination of strength and ductility, Mater. Des. 168 (2019) 107640.
- [50] J.W. Christian, The Theory of Transformations in Metals and Alloys, Newnes, 2002.